Solar Physics
DOI: 10.1007/•••••-•••-•••-••••-•

Forecasting Solar Flares by Data Assimilation in Sandpile Models.

Solar Physics

Christian Thibeault[1] · Antoine Strugarek[2] · Paul Charbonneau[1] · Benoit Tremblay[3]

Abstract The prediction of solar flares is still a significant challenge in space weather research, with no techniques currently capable of producing reliable forecasts performing significantly above climatology. In this paper, we present a flare forecasting technique using data assimilation coupled with computationally inexpensive cellular automata called sandpile models. Our data assimilation algorithm uses the simulated annealing method to find an optimal initial condition that reproduces well an energy-release time series. We present and empirically analyze the predictive capabilities of three sandpile models, namely the Lu and Hamilton model (LH) and two deterministically-driven models (D). Despite their stochastic elements, we show that deterministically-driven models display temporal correlations between simulated events, a needed condition for data assimilation. We present our new data assimilation algorithm and demonstrate its success in assimilating synthetic observations produced by the avalanche models themselves. We then apply our method to GOES X-Ray time series for 11 active regions having generated multiple X-class flares in the course of

✉ C. Thibeault
christian.thibeault@umontreal.ca

✉ A. Strugarek
antoine.strugarek@cea.fr

✉ P. Charbonneau
paul.charbonneau@umontreal.ca

✉ B. Tremblay
btremblay@nso.edu

[1] Departement de physique, Universite de Montreal, C.P. 6128 Succ. Centre-ville, Montreal H3C 3J7, Canada

[2] Departement d'Astrophysique/AIM, CEA/IRFU, CNRS/INSU, Univ. Paris-Saclay, Univ. de Paris, 91191 Gif-sur-Yvette, France

[3] Laboratory for Atmospheric & Space Physics, 3665 Discovery Drive, Boulder, CO 80303, U.S.A.

their lifetime. We demonstrate that for such large flares, our data assimilation scheme substantially increases the success of "All-Clear" forecasts, as compared to model climatology.

Keywords: Flares, Forecasting, Avalanche models, Data assimilation, Self-organized criticality

1. Introduction

The accurate prediction of large solar flares is one of the desired milestones in ongoing space weather research efforts. A number of semi-empirical, statistical, and/or data-driven techniques have been designed over the years, with various degrees of success. Nonetheless, none of them seem so far to be consistently doing very much better than so-called climatological forecasting, which consists in simply predicting according to empirically constructed statistical distributions. The flare forecasting exercise reported upon in Barnes *et al.* (2016) (see also Leka *et al.* (2019a) and Leka *et al.* (2019b)) is particularly interesting in quantifying the relative merits of these various techniques.

That reliable flare forecasting should prove hard to achieve is not at all surprising. The first major challenge is related to the extremely wide range of spatial and temporal scales characterizing the flaring phenomenon. This makes brute force approaches based on magnetohydrodynamical simulations extremely challenging, if not unpractical (see Cheung *et al.* (2019) for arguably the closest yet). Empirical/statistical techniques face another related challenge: the observed size distributions of flares take the form of a steep power law (e.g. Dennis (1985); Aschwanden (2011)), meaning that large flares, which are the most important to accurately forecast, are rare. Consequently, the observational statistics are dominated by small events, implying in turn that methods such as machine learning have (relatively) few examples of the largest flares available for training purposes.

The power-law shape of flare properties (peak flux, duration, total released energy) is an indication of scale invariance, which is a strong hint as to the inner workings of the flare phenomenon. Furthermore, similar power laws are constructed from stellar flare data (see Aschwanden, Stern, and Güdel (2008) and Namekata *et al.* (2017)), pointing to universality in the flaring process. This observed scale invariance has led to the consideration of flares as possibly arising from an avalanche of small reconnection events cascading across coronal loops or other magnetic structures. Lu and Hamilton (1991) and Lu *et al.* (1993) have designed the first lattice-based sandpile models capturing this avalanching process, with numerous variations on the theme subsequently proposed as explanatory frameworks for flares in general (for reviews, see Charbonneau *et al.* (2001) and Aschwanden *et al.* (2016)). A key aspect of the Lu & Hamilton proposal is that their lattice, an idealized representation of a coronal structure loading magnetic energy, autonomously reaches a critical state in response to slow external forcing, from which results scale-invariant impulsive energy release. This represents an instance of self-organized-criticality (hereafter SOC; see Bak,

Tang, and Wiesenfeld (1987) or Jensen (1998)), now understood to be a robust generator of scale-invariant behavior, including power-law size distribution for energy release events in general. Indeed, the SOC framework has been applied to phenomena as diverse as solar flares, earthquakes, lightning, and geomagnetic substorms, to name but a few (Aschwanden, 2011; Watkins *et al.*, 2016).

In the context of solar flare, the SOC hypothesis is buttressed by a physical scenario due to Parker (Parker, 1988), according to which photospheric fluid motions twist and braid the footpoints of magnetic fieldlines within coronal loops, leading to the inexorable buildup of magnetic tangential discontinuities (or current sheets) becoming unstable and releasing thermal energy in the form of what Parker dubbed nanoflares. Although originally designed as a model for coronal heating, Parker's scenario contains all required elements for scale-invariant release of magnetic stress by cascades of localized reconnection events within a coronal loop. This is the physical picture captured by the sandpile models of the general type introduced by Lu & Hamilton.

All avalanche models proposed in the flare context involve stochastic elements, either in lattice loading, avalanche triggering, and/or internal redistribution in the course of avalanches. This may lead one to expect that such models, even if they properly capture statistical flaring behavior, should be useless for prediction of individual events. For any of the aforecited sandpile models, the triggering and unfolding of the numerous small avalanches, equivalent to the more frequent, smaller flares, are indeed strongly affected by the stochastic elements embedded in the model, and so are truly unpredictable.

However, and perhaps counter-intuitively, this may not be the case for the larger avalanches. In sandpile models, large avalanches release large-scale stress patterns having built up in the lattice in response to slow external forcing, but also via the unfolding of earlier avalanches, especially the larger ones. Once they reach the self-organized critical state, sandpile models exhibit long range spatiotemporal correlations (Jensen, 1998), so that even in the presence of truly stochastic elements, the system does not behave completely stochastically. What this implies is that information useful for predicting future avalanching behavior is contained, in principle, in past avalanching behavior. How to extract that information then becomes the key challenge.

Data assimilation is one attractive possibility. In short, the idea is to use past observations to adjust the state of an underlying physical model to best reproduce these observations, yielding an "optimal" initial condition for model-based forecasting. Such procedures have been extensively used for (earthly) weather forecasts. Bélanger, Vincent, and Charbonneau (2007) and Strugarek and Charbonneau (2014) have presented proof-of-concept and exploratory results on the use of various data assimilation methods in the context of sandpile models for flares. These latter authors, in particular, have shown an example of successful assimilation of both synthetic data as well as GOES X-Ray flux time series. This prior work is the motivation and starting point of the work reported upon here.

In this paper, we first introduce in section 2 the three sandpile models used in our analysis, namely the Lu and Hamilton model (LH) and two deterministically driven models (D), taken from Strugarek and Charbonneau (2014). In section 3,

we present empirical analyses and comparison of the predictive potential of these three models. In section 4, we present our data assimilation protocol and our results in assimilating synthetic observations produced by the sandpile models. In section 5 we apply our assimilation scheme to a set of GOES X-Ray flux time series, and demonstrate that data assimilation yields a substantial improvement in forecasting skill for large avalanches, over and above model climatology. We conclude in 6 by summarizing our method and results, and outlining the path to future improvements.

2. Sandpile models for solar flares

Sandpile (or avalanche) models are cellular automata that can be used to represent the flaring solar corona in a highly simplified view. Despite their simplicity, they capture at some level the threshold dynamics and disparity of spatial and temporal scales characterizing the flaring phenomena, and reproduce reasonably well the power-law size distributions of solar flares. They also draw physical support from the nanoflare picture proposed by Parker (1988). In comparison to MHD models of coronal magnetic fields, sandpile models are computationally inexpensive and thus, in principle, can be more easily coupled with data assimilation methods. For detailed reviews on sandpile models for solar flares, we refer the reader to Charbonneau *et al.* (2001) and Aschwanden *et al.* (2016).

2.1. The Lu and Hamilton Model

The first sandpile model of solar flares was published by Lu and Hamilton in 1991 (Lu and Hamilton, 1991). As such, it is often considered as the canonical avalanche models for solar flares, which we denote as "LH" hereafter. Here, we use a 2D Cartesian lattice version of this model, with 48×48 nodes each assigned a real number denoted $A^n_{i,j}$, where n is a discrete time index and (i, j) are its lattice coordinates. The driving of the lattice takes place via addition of a small increment value δA on a single randomly selected node, at every non-avalanching temporal iteration. The value of δA is randomly selected through a uniform distribution between -0.2 and 0.8. The boundary of the lattice is kept at $A = 0$.

The stability of a node is determined by its local curvature, approximated as:

$$\Delta A^n_{i,j} \equiv A^n_{i,j} - \frac{1}{4}\sum_{k=1}^{4} A^n_k \ , \tag{1}$$

where k denotes each nearest neighbor of the node (i, j). Once $|\Delta A^n_{i,j}|$ exceeds a predetermined threshold Z_c, driving is suspended and redistribution occurs to restore stability. This is achieved by transferring an amount of nodal value from the unstable node (i, j) to each neighbor according to the following rules:

$$A^{n+1}_{i,j} = A^n_{i,j} - \frac{4}{5}Z \ , \tag{2}$$

$$A^{n+1}_{i\pm1,j\pm1} = A^{n}_{i\pm1,j\pm1} + \frac{1}{5}Z \ , \tag{3}$$

where $Z \equiv Z_c \Delta A^n_{i,j}/|\Delta A^n_{i,j}|$. This process is deterministic and conservative, meaning that the total amount of nodal value is conserved during the redistribution. This redistribution can cause one or more neighbouring nodes to exceed the stability threshold, in which case redistribution is applied anew to these unstable nodes, and so on until stability is everywhere restored. Only then does driving resumes ("stop-and-go" sandpile). These chain reactions of redistribution events are what we call *avalanches*, and represent the model equivalent of a solar flare.

Since the nodal value $A^n_{i,j}$ is generally associated with a measure of the magnetic twist in a coronal loop, the usual measure of the magnetic energy of the lattice is defined by:

$$E^n = \sum_{i,j} A^2_{i,j} \ , \tag{4}$$

where we sum on all nodes of the lattice. Each redistribution will therefore cause a decrease in lattice energy by the amount:

$$\Delta e^n_{i,j} = \frac{4}{5e_0}\left(2\frac{|\Delta A^n_{i,j}|}{Z_c} - 1\right) Z_c^2 \ , \tag{5}$$

where e_0 is the energy liberated by a single node exceeding the stability threshold by an infinitesimal amount, expressed as:

$$e_0 = \frac{4Z_c^2}{5} \ . \tag{6}$$

In all that follows, we use a threshold value $Z_c = 2$, and the above quantity as the unit to express energy released by avalanches of all sizes.

The total energy released by the lattice per iteration (ΔE^n_r) is equal to the total energy loss of all redistributing nodes. Note that other physical interpretations of the lattice nodal variable can lead to other measures of energy release in avalanche models (for a more in-depth discussion, see chapter 12 in Aschwanden 2013 and Farhang, Wheatland, and Safari 2019).

Sandpile models describe the evolution of a system on two characteristic timescales, the forcing timescale corresponding to the typical evolution time of an active region, of the order of hours to days, and the eruption timescale corresponding to the impulsive flare of the order of seconds. In what follows, the total energy released by an avalanche in a sandpile model will be directly compared to the peak energy flux of a solar flare in the X-Ray domain, as the subsequent cooling of the flaring region is not accounted for in the sandpile model.

2.2. The Deterministically Driven Sandpile Model

A deterministically driven model in the context of solar flare simulations was first proposed by Strugarek *et al.* (2014), notably inspired by deterministic driving schemes used for seismic faults (Olami, Feder, and Christensen, 1992) and geomagnetic substorms (Liu *et al.*, 2006; Vallières-Nollet *et al.*, 2010). The lattice is driven globally, through the following deterministic forcing rule:

$$A_{i,j}^{n+1} = A_{i,j}^{n} \times (1+\epsilon), \quad \epsilon \ll 1, \quad \forall (i,j) \ , \tag{7}$$

where $\epsilon \ll 1$ is the driving rate. We use a value $\epsilon = 10^{-5}$ and denote these models as "D" in what follows.

The stability criterion remains the same as in the LH model (equation (1)): once the curvature of a node exceeds a threshold Z_c, redistribution occurs evenly among all neighbors as in the LH models, but with random loss of nodal value induced per redistribution:

$$A_{i,j}^{n+1} = A_{i,j}^{n} - \frac{4}{5} Z \ , \tag{8}$$

$$A_{i\pm1,j\pm1}^{n+1} = A_{i\pm1,j\pm1}^{n} + \frac{r_0}{5} Z \ , \tag{9}$$

where r_0 is extracted from a uniform distribution spanning $[D_{nc}, 1]$. This redistribution rule is non-conservative, as each redistribution now involves a random loss of nodal value from the lattice. As a consequence, the stochastic element enters the unfolding of avalanches, rather than in the driving mechanism as in the LH model.

As argued in Strugarek *et al.* (2014), the deterministic driving introduced above can be (loosely) interpreted as a global twisting of a coronal loop by photospheric flows coherent on scales commensurate with the loop's diameter. In what follows we consider two versions of deterministically-driven models encapsulating different levels of stochasticity (corresponding to model D2 and D3 in Strugarek and Charbonneau 2014). The first, hereafter dubbed Model D09, uses a conservation parameter $D_{nc} = 0.9$ and is considered a mildly non-conservative model. The second, Model D01, is a more strongly non-conservative model, with $D_{nc} = 0.1$, and thus introduces a larger degree of stochasticity in the unfolding of its avalanches.

2.3. Avalanching properties of LH and D models

We illustrate typical energy release time series for models LH and D01 in the top panels of Figure 1. Model D01 clearly tends to produce much larger avalanches than model LH. To explicitly account for the large separation of timescales between the release of energy in solar flares and their waiting times, we follow Lu *et al.* (1993) and compress avalanches into discrete events (as shown in the bottom panels of Figure 1), each representing the sum of all energy released during an avalanche. Since we wish to focus on large avalanches, we only retain

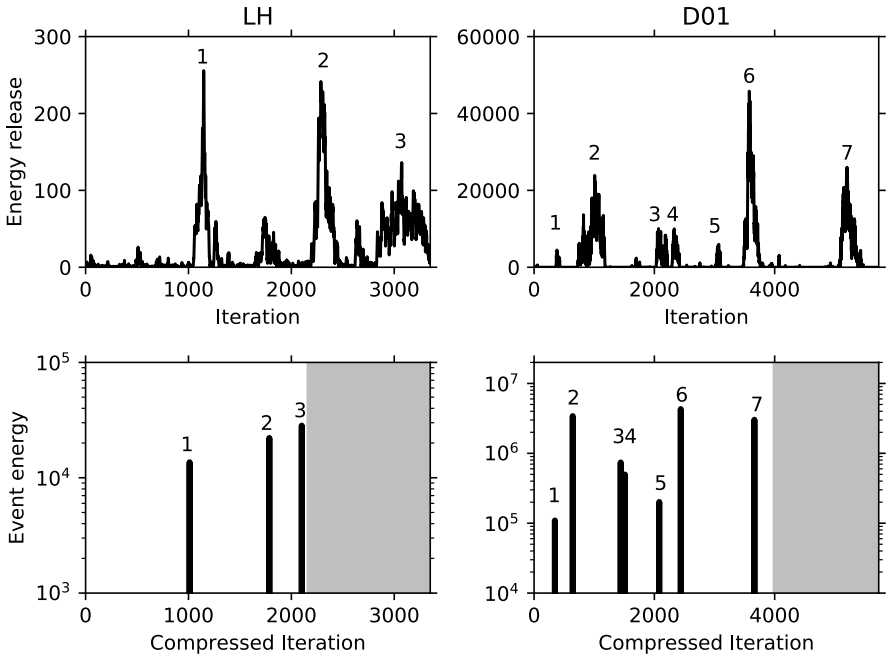

Figure 1. Top: Energy release time series for model LH (left) and D01 (right). Bottom: Compression of the same energy release time series, where each line represents the total energy released during a large avalanche (over 10^5 for model D01 and 10^4 for the LH model). Here as on all subsequent plots showing energy release time series, energy is measured in units of e_0 (viz. eq. (6)). Individual avalanches are labelled in each panel (1 to 3 for left panels, 1 to 7 for right panels). The grey area is added to represent the iterations lost during the compression algorithm. Compressed avalanches below threshold are not numbered.

avalanches preceding a preset threshold, which we (somewhat arbitrarily) set at 10^5 for models D01 and D09, and 10^4 for the LH model.

Figure 2 shows histograms of waiting time between events above a given threshold for models LH, D09 and D01. In model LH, a clear exponential distribution is seen, indicative of a stationary Poisson process (Wheatland, 2000). This result is expected for model LH, which triggers avalanches using a random driver. In the D models, the distribution could be approximated to an exponential law for intermediate-size events. For larger events, model D01 departs from this exponential distribution.

3. Predictive capabilities of avalanche models

3.1. Robustness of large avalanches

Strugarek and Charbonneau (2014) showed with a limited exploration that deterministically driven models have a strong potential to robustly predict large

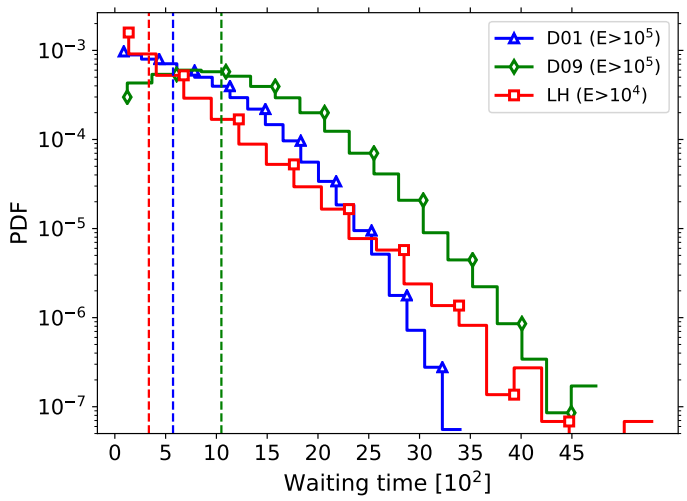

Figure 2. Waiting time distribution between avalanching events releasing energy over 10^4 (in e_0 units) for Model LH and over 10^5 for Model D01 and D09, with median waiting times shown by dashed vertical lines.

events compared to LH models. We further expand their analysis to systematically characterize this ability. From one fixed initial condition preceding a large avalanche, we used 1000 different random-number sequences to drive the LH model until an avalanche is triggered. Likewise, we use 1000 distinct random number sequences to control avalanching behaviour in the deterministically-driven D01 and D09 models. The distribution of energy released in the first avalanche in all the 1000 runs is presented in the top panel of Figure 3. In this example, models D01 and D09 both have a very high tendency to produce large avalanches, regardless of their random-number sequences. This suggests that a pre-existing stress pattern in the lattice is an important factor in producing a large avalanche. In the case of the LH model, the distribution is much wider, indicating a larger sensitivity to the random-number sequence in triggering a large avalanche.

We then investigated how these distributions of events change with respect to different initial conditions preceding avalanches of different sizes. To do so, we produced 1000 distributions of energy released from initial conditions preceding large avalanches, such as the ones presented in top panel of Figure 3. With each of these distributions, we extract the average and relative standard deviation of the energy release. The bottom panel of Figure 3 shows the relationship between these two extracted parameters. In general, the distribution of events tends to be more concentrated as the average energy released increases for all models. The cutoff of the LH model to events higher than 10^5 is a characteristic of the model itself, which tends to produce smaller events. For the D models, the standard deviation of the distributions drops for events higher than 10^6, especially in the case of model D09. This confirms previous findings that D models tends to favor large avalanches in its predictive capabilities.

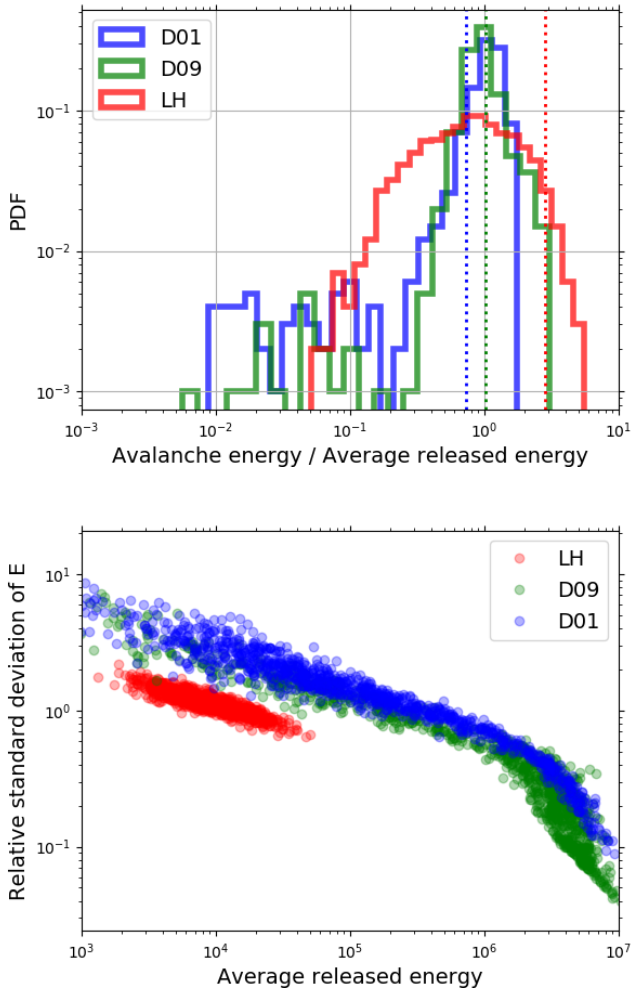

Figure 3. Top: Probability density function (PDF) of energy released from 1000 avalanches produced from the same initial condition, but with varying random-number sequences. The initial condition is chosen to precede a large avalanche. Bottom: Relative standard deviations of 1000 distributions of energy released (E) such as the one presented in the top panel of this figure, with respect to the average energy released of each distribution.

3.2. Short-term correlations between large events

The results shown in the previous section already suggest that the timing of a large avalanche is dictated by the stress patterns established across the lattice by previous avalanches. To assess whether data assimilation can be successfully coupled to sandpile models, we verified that these models also contain short-term correlations between large events. We also characterized the memory timescale associated with stress patterns. Towards this end, we first construct a composite

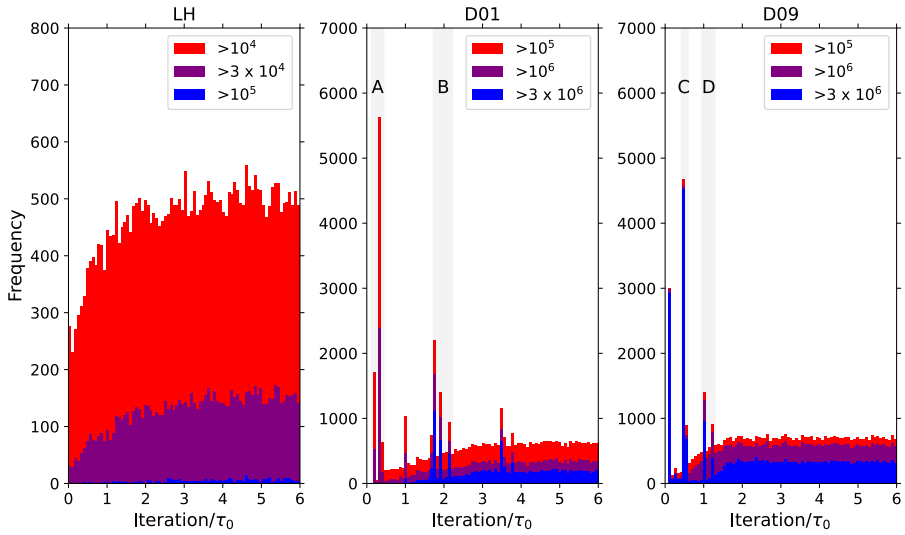

Figure 4. Occurence time for large avalanching events (over 10^4 for the LH model and over 10^5 expressed as before in units of e_0, for both D models) from 10 000 models runs, each with identical initial conditions but with varying random-number sequences. The grey highlighted areas, labeled as A, B, C and D are time windows used to analyse correlations between the timing of large events.

time series by superposing the compressed energy release time series of 10 000 model runs, each using the same initial condition but with a distinct stream of random-number for driving (LH) or redistribution (D01, D09). Any large peak in such a composite time series is indicative of preferred time for avalanching, i.e., memory.

Such composite time series are shown in Figure 4, for models LH (left), D01 (middle) and D09 (right). In all cases, the time axis is normalized by the median waiting time (τ_0) between events larger than 10^5 for D models and 10^4 for the LH model (these characteristic times are also indicated in Figure 2). In the case of the LH model (leftmost panel of Figure 4), we see no preferential timing of large events. These results are consistent with previous findings regarding the low predictive capabilities of the LH model (Strugarek and Charbonneau, 2014). For the deterministically driven model D01 (middle panel), the results show clear peaks in the timing of large events. These peaks cluster within time windows smaller than $\tau_0/2$ and persist until up to $4\tau_0$. It suggests that the lattice contains stress patterns that tend to produce large avalanches at specific times. The lack of avalanches prior to the very first peak shows here that avalanches of smaller energy than the threshold and occurring before the first peak do not affect significantly its timing.

Further analysis shows that 58% of D01 simulations that produced large events ($> 10^5$) in the B window (from $1.75\tau_0$ to $2.15\tau_0$) also produced large events in the A window, the initial phases of the simulation. Model D01 therefore shows short-term correlations between events, meaning that large events produced in one time window will coherently affect the timing of future events over a time

interval spanning up to 4 median wait time. In the case of model D09, the peaks are composed mainly of very large events ($> 3 \times 10^6$, in blue). They persist on a shorter time window of around $1.2\tau_0$. This model also shows a lower correlation between groups of large events. For example, only 33% of runs that produced large events in the D time window also produced large events in the C window. This shows a lower and less consistent correlation between the timing of large events, in comparison with model D01.

In summary, we have shown significant differences between the "memory" in our three avalanche models, even though all generate power-law PDFs with similar logarithmic slopes for their size measures, as well as roughly similar waiting time distributions. We have also shown that significant short-term correlations exist between large avalanches for Model D01. Conversely, the D09 and LH models show little to no short-term correlations between large-events. The timing distributions shown in Figure 4 are representative of tens of such analyses from different initial conditions, and thus represent robust features of each model. Since the LH model does not show promising predictive capabilities, we chose to omit this model in its coupling with data assimilation in what follows[1].

4. Data assimilation

Data assimilation consists of using a set of external data to alter the internal state of a model until it reproduces the external data satisfactorily. It can be used to derive the most realistic parameters of a reduced model, to test if a given model can accommodate a given set of data, or to develop a physical model compatible with a given series of observations that can then be used to carry out predictions (*e.g.* Hung *et al.* 2017). We are interested in this paper in the latter application of data assimilation for large and rare solar flares.

The use of data assimilation to fit a model to observational data has been extensively used in many fields, notably in meteorological forecasting (Kalnay, 2002). The general idea is to fit a simulated time series to a time window of observational data by adjusting initial conditions of the model. To achieve this, gradient descent methods, such as 4D-var, are typically used to minimize a cost function $\mathcal{J}$ that measures the distance between the observed and modelled time series. In the case of avalanche models for solar flares, data assimilation is particularly challenging due to: (1) the strongly nonlinear relationship (due to threshold dynamics) between the model's internal state and output, (2) the stochastic and discrete nature of the model output, and (3) the degenerate nature of the model-to-output relationship, i.e., many distinct lattice configurations can yield similar avalanching behavior. We present in the following section an overview of the data assimilation procedure we have designed to address these challenges.

[1]Morales and Santos (2020) show that lattice mass (or energy) is in fact a good predictor of large avalanche in the LH model. However, this quantity is not directly accessible observationally, and is thus of limited value for operational forecasting purposes.

4.1. Data assimilation Procedure

4.1.1. Data to assimilate

The data to be assimilated consists of a series of discrete events characterized by an amplitude and an occurrence time (see e.g. bottom panels in Figure 1). The first type of data we will assimilate is *synthetic data* (see §4.2), produced independently by the sandpile model. Synthetic data can be used to validate the data assimilation procedure with data that we know can be produced by the model itself. More specifically, we use synthetic data to determine optimal numerical values for the various parameters defining our cost function and controlling the minimization algorithm. We defer assimilation of GOES X-Ray flux data to §5.

4.1.2. Comparing two sets of discrete events: design of an efficient cost function

The fundamental quantity we want to assimilate over a preset temporal window (hereafter the *assimilation window*) is a series of discrete events, which call here *reference data*. The output of the avalanche model is also a series of discrete events, which we refer to as *model data*. Simple least-squares minimization is impractical due to the discrete nature of these data. We thus developed a dedicated cost function $\mathcal{J}$ designed to compare the distance between two series of discrete events (Bélanger, Vincent, and Charbonneau, 2007).

Our primary goal is to accurately reproduce the largest events in a given time series. We also do not want to miss any large events, as these set the long-range spatial correlations across the lattice that confer predictability to the model, despite its stochastic elements. Finally, false alarms also need to be avoided during the assimilation process, as they will likely decrease the predictive potential of the assimilated model. For each event in the reference data and in the model data, we check whether it is a *match*, a *miss* or a *false alarm*. Two events are considered to match when the model event occurs within a small time-window (here 400 model iterations) around the reference event, and with an energy in $[E_0/2, 2E_0]$ (where E_0 is the energy of the reference event). We illustrate the distinction between matched, missed and false alarm events in Figure 5. Note that our match criterion is quite demanding, any event outside the gray boxes is considered a miss, including the rightmost pair of observation and assimilated events despite their similar timing.

The cost function $\mathcal{J}$ is then defined as

$$\mathcal{J} = 1 - \left(\alpha \sum_{\text{match}} \frac{E_0}{E_{\text{tot}}} - \beta \sum_{\text{miss}} \frac{E_0}{E_{\text{tot}}} - \gamma \sum_{\text{False Alarm}} \frac{E_i}{E_{\text{tot}}} \right) , \tag{10}$$

where $E_{\text{tot}} = \sum E_0$ is the total energy released in the reference data over the assimilation window, E_i is the energy of events in the model data, and α, β and γ are adjustable weights that we set here to 1, 0.5 and 0.25. This cost

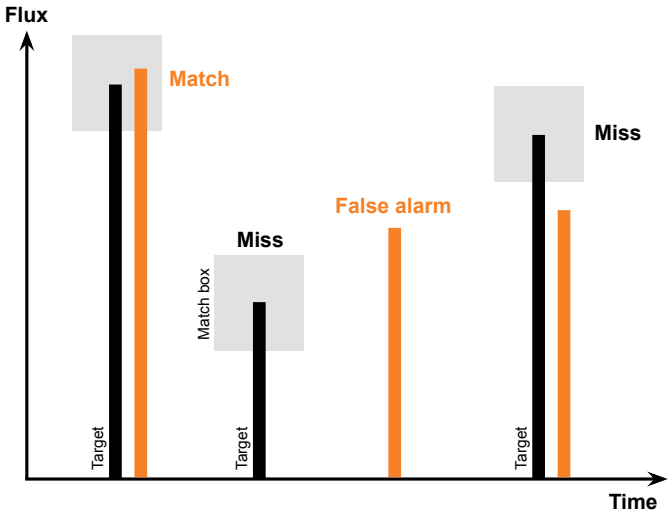

Figure 5. Illustration of our definition of a match, miss and false alarm used in our cost function between the reference (shown in black) and model data (shown in orange). The gray squares represent areas in which the model data is considered a match.

function thus gives more weight to large events that we want to assimilate and predict most reliably. It also gives more weight to matching events ($\alpha = 1$) than missed events ($\beta = 0.5$), and finally less weight to false alarms ($\gamma = 0.25$). If each of the reference data is matched with a model data within the match box, $\mathcal{J} = 0$. Conversely, if none of the reference events are matched by the model events, $\mathcal{J} \sim 1.75$ (no match, all data events are considered as false alarms and all reference events as misses).

The cost function (10) is only one example of how to design a cost function to compare two discrete series of events. We tested various flavors of $\mathcal{J}$, *e.g.* by varying the coefficients α, β and γ and by using the logarithm of the fractional energy of events $E_0/E_{\rm tot}$ and did not find any significant change in the results presented here.

4.1.3. Minimization of the cost function

In order to minimize the cost function (10), several optimization techniques can be used. Before selecting a minimization algorithm, one must beforehand define which part of the model is allowed to evolve during the process. Here, we do not want to alter the avalanche model's internal parameters (threshold Z_c driving rate ϵ, etc.) in order to maintain solar-like statistics. The only option left is then the initial condition of the sandpile, which is typically of size $N = N_x \times N_y \sim 10^3$. Such a large set of control parameters slows down the assimilation process. In this work, we make use of the eigenvalue decomposition of the lattice nodel variable, i.e., of the sandpile model itself. This consists in finding a basis of decomposition for states of the sandpile models. Any sandpile state can be decomposed on a basis of $N_x \times N_y$ (here 48×48) eigenfunctions. Here we automatically generate

such a basis by diagonalizing the covariance matrix of our model (see Strugarek *et al.* 2017 for more details), and we limit the number of eigenvalues to assimilate to 50. This effectively greatly reduces the dimension of our minimization while maintaining our ability to minimize adequately our cost function. The details of this technique can be found in Hung *et al.* (2017) in the context of the prediction of the solar cycle, and in Strugarek *et al.* (2017) in the context of flare forecasting with sandpile models.

The minimization of the cost function can be realized through standard down-gradient algorithms; advanced 4D-Var method using an adjoint code to estimate the gradient of the cost function (Bélanger, Vincent, and Charbonneau, 2007) (and hence significantly reducing the convergence time of the minimization); or more generic and costly algorithm such as simulated annealing to avoid local minima traps by allowing up-gradient exploration. We tested each of these methods. The adjoint of the sandpile model was automatically generated using the Tapenade software (Pascual and Hascoët, 2006). We used the simulated annealing algorithm implemented in Numerical Recipes (Press *et al.*, 1992). We found by employing these different approaches that only the simulated annealing algorithm was able to robustly succeed. Indeed, the cost function (10) presents numerous local minima, and most down-gradient minimization methods are not able to find a sufficiently good minimum. An alternative approach could make use of neural networks to minimize $\mathcal{J}$, which we leave for future work.

The simulated annealing method allows occasional up-gradient explorations with a probability that depends on a parameter T_s that represents the temperature, in analogy to annealing in metallurgy. In this work, T_s is initialized at 10, and is then decreased over 19 iterations until it reaches 5×10^{-2}. As proposed in Numerical Recipes (Press *et al.*, 1992), each iteration of the simulated annealing operates on a downhill simplex method. Here we use 20 iterations of downhill simplex for each simulated annealing iteration. The choice of the cooling schedule of T_s and the number of iterations for both algorithms have been found empirically to achieve satisfying results while maintaining relatively high calculation speed.

4.2. Quality of the data assimilation procedure

Figure 6 highlights three examples of the evolution of the cost function $\mathcal{J}$ for Model D01 undergoing our minimization algorithm presented above. The upper panel traces the evolution of the up-gradient step probability, and the lower panel the evolution of the cost function. In the lower panel, 100 different simulated annealing runs are presented as grey lines. The median, worst and best runs are respectively shown in green, red and blue. In the initial phase of the minimization, the temperature T_s is high enough for up-gradient exploration to occur fairly frequently, as seen in the upper panel. This can be seen in the initial phase of the worst (red) and median (green) runs, with a clear up-gradient step taken at the fifth simulated annealing step. As the temperature diminishes, the cost function stabilizes to a local minimum. As can be seen on the cost function histogram plotted at bottom right, the end result of these 100 minimization results contains two main groups, one with higher final cost functions

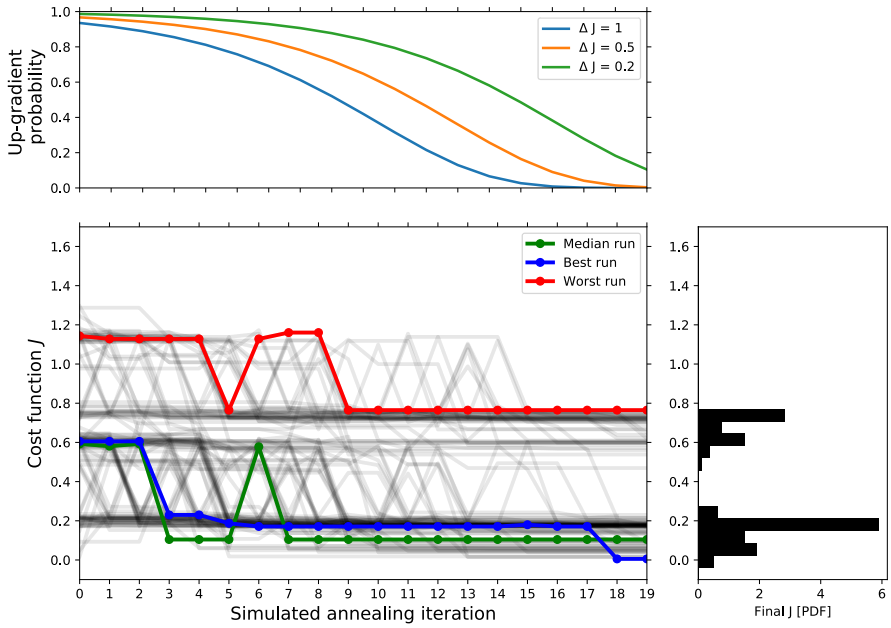

Figure 6. Evolution of the cost function during 100 optimization runs of Model D01 on a single synthetic observation. The grey lines represent the results of all 100 simulated annealing runs, and the blue, green and red lines highlights the best, median and worst run respectively. The up-gradient probability of the algorithm is shown in the upper panel on the same timescale. The histogram on the right shows the distribution of final cost function values for the 100 runs.

of $\mathcal{J} \sim 0.5 - 0.7$ and the other with more successful runs of $\mathcal{J} \sim 0 - 0.2$. Such grouping of results are quite frequent in our minimization outputs, and result in part from the discrete nature of the penalties produced by misses and false alarms in the design of the cost function $\mathcal{J}$.

We show in Figure 7 the resulting compressed time series of avalanche energy release at the end of data assimilation. The color-code of Fig. 6 has been retained and we illustrate the models resulting from the best (blue, top left), median (green, top right) and worst (red, bottom) assimilation runs. In the first example, the assimilated run (blue vertical line segments) succeeds in capturing the five largest synthetic reference events (black), leaving as "false alarms" only two small events barely above our 10^5 threshold (around iteration 600, and around iteration 3500 right before the last matched event in the window). This leads to a near-perfect cost function of $J = 0.0056$. In the second example (green peaks), two low-energy reference events are missed which leads to a cost function of $J = 0.17$. Finally, in the third example (red peaks), only two reference events were captured, and three were missed. These large missed events lead to a large increase in our cost function, here $J = 0.76$, as per the high penalty assigned to misses in our cost function design (viz. §4.1.2). The three false alarms also contribute, to a lesser extent, to this higher cost function (misses have twice the weight as false alarms). These three examples show variations of assimilation

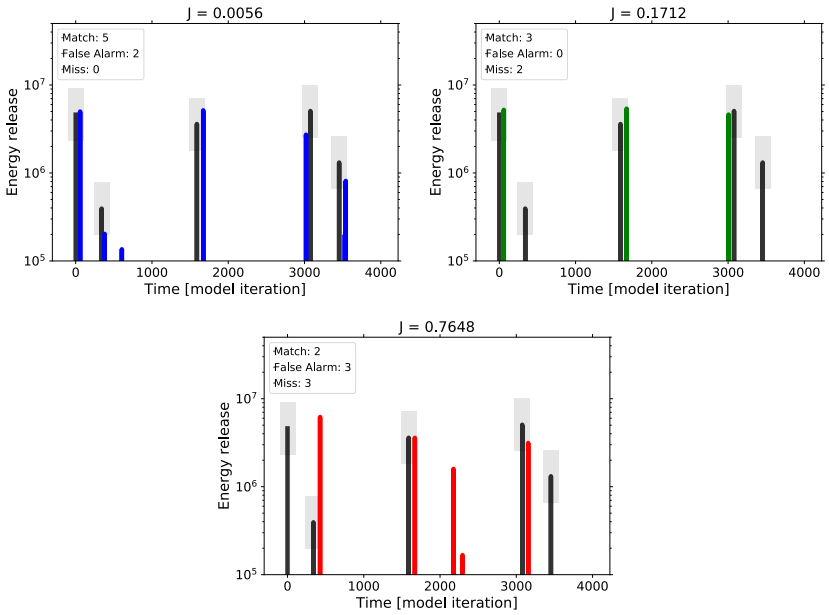

Figure 7. Event energy time series of the best (top left, blue), median (top right, green) and worst (right, red) output of 100 data assimilation runs using Model D01 on a common synthetic data. These three examples corresponds to the output of the same color-highlighted examples shown in Figure 6

results on a single synthetic observation, but the results also fairly depend on the synthetic data being assimilated.

We now characterize the average performance of our data assimilation process. We produce randomly 100 synthetic observation timeseries, which we attempt to assimilate. For each synthetic observation, we run 100 assimilation runs. The results are summarized in Table 1. In the case of model D01 we find that the assimilated runs produce a satisfying cost function $\mathcal{J} \leq 0.1$ for 6% of the assimilation runs. On average, the assimilated run rather give results with a cost function between 0.2 and 1. Conversely, if one randomly generates sequences of the avalanche models instead of using the assimilated runs, the average cost function increases significantly, and a satisfying cost function $\mathcal{J} \leq 0.1$ is achieved for only 1% of the random sample. Our assimilated runs therefore clearly show significantly better results than the randomly generated initial conditions. Most importantly, the low computational cost of assimilating these sandpile models allows us to easily repeat the assimilation process until an acceptable ($\mathcal{J} \leq 0.1$) assimilation is obtained, to later be used for forecasting.

We further characterize the data assimilation performance by the cumulative distribution of the best cost function achieved for each observation, denoted as J_{min}, and shown in Figure 8 for models D01 and D09. Both these models clearly outperform unassimilated runs from a random initial condition (shown as dotted lines). Only around 17% of observations produce a J_{min} close to 0 for model D01, and 36% for model D09. A cost function of 0 is difficult to achieve

Table 1. Results of all 10000 data assimilation runs ([%])

J range	D01 Assimilated	D09 Assimilated	D01 Random	D09 Random
$[0, 0.1]$	6.48	5.90	1.15	0.10
$[0.1, 0.2]$	9.99	7.65	0.36	0.17
$[0.2, 0.5]$	40.67	43.17	2.18	1.39
$[0.5, 1]$	42.15	43.00	15.38	11.15
> 1	0.71	0.25	80.93	87.18

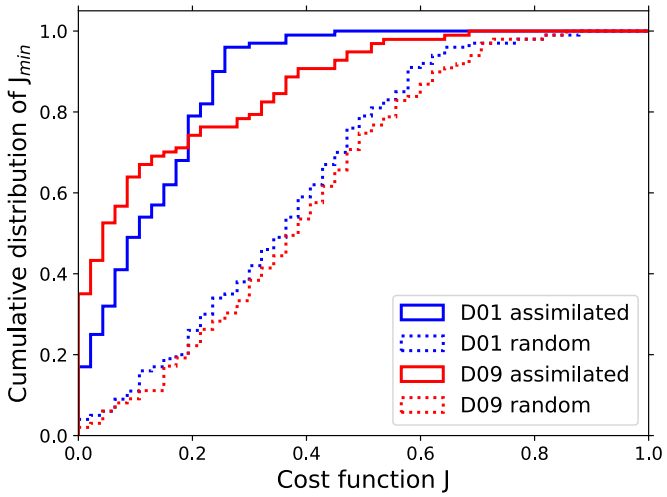

Figure 8. Cumulative distribution of the best results (J_{min}) on each of the 100 synthetic observations. The dashed lines represent the results generated from random states, whereas the full lines are from assimilated states.

for most observations with our current data assimilation algorithm, especially for those with the most events to assimilate. Model D09 outperforms Model D01 until around $J_{min} = 0.21$, but model D01 seems more robust with its best results, with all of them being at least under $J_{min} = 0.5$.

In all cases, the assimilated runs clearly outperforms randomly generated sequences. Even though the above results suggest that model D09 outperforms to some extent model D01 in yielding very low values for the cost functions, we also recall from §3 that model D01 has a much longer prediction horizon (cf. middle and bottom panels of Fig. 4). Consequently, all forecasting experiments reported upon in the remainder of this paper make use of model D01.

4.3. Predictive capabilities on synthetic data

Before turning to real solar flaring data we first verify that the data assimilation process described above increases the forecasting skill over forecasts performed using a random (unassimilated) initial condition. The latter captures the model "climatology", i.e., the mean statistical behavior in the triggering of avalanches.

We adopt the "all-clear" forecasting paradigm described in Barnes and Leka (2008) (see also Barnes *et al.* 2016). This is a binary forecast which is defined as follows: given a forecasting window $t \in [0, T]$ extending from the present ($t = 0$) to some future time ($t = T$), will at least one avalanche/flare of energy $E > E^*$ occur at any time within this window. We measure forecasting performance through a simple "Rate Correct" (RC) measures:

$$\mathrm{RC} = \frac{\mathrm{TP} + \mathrm{TN}}{N} \ . \tag{11}$$

where TP is the count of true positives (an avalanche was predicted in the forecasting window and did occur), TN the count of true negatives (no avalanche was predicted and none occurred), and N is the total number of forecasts attempts. We extract 250 non-overlapping 4000-iteration long segment of energy release compressed time series from an extended simulation run of model D01. We then use the first 2000 iterations of each as the assimilation window, and the subsequent portion of the segments as target. For each such dataset, we run our data assimilation scheme 100 times using 100 distinct random initial conditions, and group the resulting initial conditions in terms of the cost function values attained. For each member of each group for each synthetic dataset, we then perform an ensemble of 10^4 statistically-independent all-clear forecasts using the same assimilated initial condition but distinct random number streams controlling nodal variable losses during avalanches. The Rate Correct statistics presented below are thus based on a total of anywhere from 10^4 up to $N = 10^6$ of such forecasts.

The left panel of Figure 9 displays the variations of the Rate Correct measure as function of the threshold (energy lower limit) values E^* (measured in units of e_0, viz. eq. 6) imposed to observations within the all-clear forecast window. The latter is here of a fixed duration of $T = 569$ model iterations, corresponding to the mean wait time for avalanches having energies larger than $E^* = 10^5$. The blue dots show the model climatology, constructed by using an unassimilated initial condition as input. Other colors indicate forecasting performance for ensembles of assimilation runs increasingly stringent on the cost function value deemed acceptable to be included in the forecast ensemble, as labeled. At low E^* all ensembles yield a rate correct of 0.5, consistent with the median waiting time, and consistent with the notion that our forecasting scheme is not expected to perform well for small avalanches, where stochasticity dominates the avalanching behavior (viz. Fig. 4). At very high $E^* \simeq 10^7$, avalanches are very rare in both target and forecast time series, so all forecast inevitably converge to RC$\simeq$ 1. However, for the large avalanches in the approximate range $10^6 \leq E^* \leq 5 \times 10^6$, assimilated initial conditions with cost function $J < 0.0001$ improve the all-clear forecasting performance by some 20% to 30%

The right panel of Figure 9 displays the results of the same ensemble of forecasting experiments, but now as a function of the extent of the forecast window (T), at fixed threshold energy $E^* = 5 \times 10^6$. At very small T the probability of producing a large avalanche is small, so all ensembles perform well (RC$\rightarrow$ 1) by forecasting "no avalanche". At T approaches the median waiting time for

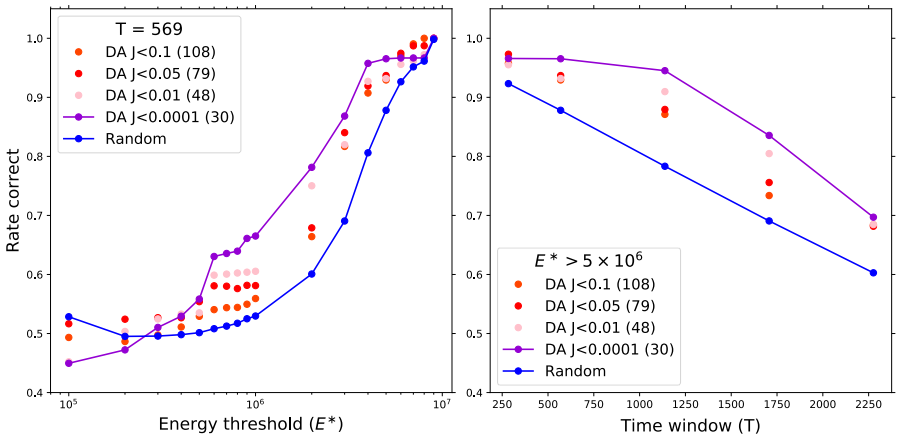

Figure 9. "All clear" forecasting performance on synthetic data. The left panels shows the variation of our rate correct measure (eq. 11) as a function of target avalanche energy threshold, expressed in units of e_0 (viz. eq. 6) over an "All-Clear" forecasting window of $T = 569$ model iterations. The right panel shows an equivalent plot, but now as a function forecasting window for a fixed target avalanche energy threshold of $E^* > 5 \times 10^6$. The color scheme identifies the range of cost function values used to select assimilated initial conditions for forecasting, as labeled, with the corresponding number of members in each ensemble given in parentheses. The blue dots and line refer to forecasts produced from a random initial condition, which defines our model climatology (see text).

this threshold value of E^*, all ensembles tend towards RC$\simeq$ 0.5. In between, assimilated runs with $J < 0.0001$ (purple) again outperform the climatological forecast (random, in blue) by up to 30%.

5. Forecasting large flares from GOES X-Ray flux time series

We now turn to the assimilation and prediction of solar flare data. We use again model D01 for all results presented in this section, in views of its superior predictivity level demonstrated in §3 (viz. Fig. 4).

Our scheme requires information on past flaring behavior in order to forecast future flaring. We opted to secure such a discrete series of flaring events from the continuous monitoring of the Sun in X-ray by the Geostationary Operational Environmental Satellites (GOES). The sandpile model (Section 2) can be conceptually related to the magnetic field overlying a single active region. The GOES timeseries, on the other hand, are obtained from the full solar disk and thus intertwine flaring events from different active regions. As a first selection step, we identify past epochs of solar activity when large flares (at least four flares of GOES class X and above) were triggered by only one predominant active region of the Sun. Based on these criteria we identified 11 past epochs with strong flaring activity arising from a single, large active region. These are listed in Table 2, and sample various phases of the solar activity cycle, as shown on Fig. 10.

Table 2. Selected observed active regions.

AR number	Time period	Maximum Flux [10^{-4} W/m^2]	Number of Flares X	M	C
5312	1989/01/06 - 1989/01/20	2.3	6	33	12
5395	1989/03/05 - 1989/03/19	15.0	11	48	48
6063	1990/05/11 - 1990/05/24	9.3	5	8	10
6538	1991/03/05 - 1991/03/17	5.5	5	17	38
6545	1991/03/11 - 1991/03/22	3.9	6	16	35
6555	1991/03/17 - 1991/03/31	9.4	7	28	44
6659	1991/06/01 - 1991/06/17	12.0	6	28	38
10486	2003/10/22 - 2003/11/05	28.0	7	20	16
10649	2004/07/12 - 2004/07/24	3.6	6	10	46
10808	2005/09/07 - 2005/09/19	17.0	10	20	47
12192	2014/10/16 - 2014/11/01	3.1	6	32	74

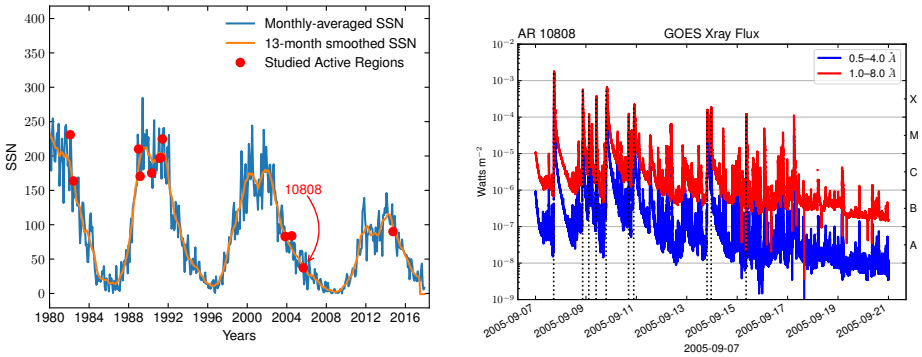

Figure 10. *Left*: Monthly-averaged (blue) and 13-month smoothed (orange) sunspot number (SSN) of the past 36 years (data from SILSO, Royal Observatory of Belgium, Brussels). The identified active regions reported in Table 2 are labelled by the red circles. *Right*: GOES time series for AR 10808, with the 6 flares of class X identified in the Heliospheric Events Knowledgebase, indicated as vertical dotted lines. The two channels of the GOES XRS instrument are shown in blue (0.5-4 Å) and red (1-8 Å).

For each epoch, a series of event can be constructed by querying the Heliospheric Events Knowledgebase (HEK), or by identifying flares from the GOES X-ray flux in the 1-8Å band following the algorithm detailed in Aschwanden and Freeland (2012). An example of the two types of series of events is show in Fig. 10 for the active region AR 10808. In the following we will only use the time series constructed from the HEK, as it allows to select only flares produced by a given active region. The corresponding list of events (time and peak flux), plotted as vertical dotted lines on Fig. 10 is treated as the observational counterpart to the avalanche model's compressed time series for energy release (viz. Fig. 1).

Our next task is to match the temporal and flux scale of GOES observations to their equivalent in the avalanche model. We first threshold the 1-8Å GOES time series to retain only flares of class X, and establish a linear scaling between peak flux measured by GOES to (compressed) peak energy from the model, matching

the most intense GOES flare in Table 2 to 5×10^6, the largest avalanche energy produced by a typical extended model run. Next we convert the GOES time stamps to model iteration by requiring that the median inter-event wait time matches approximately the median wait time of the model. This is done by multiplying the GOES time stamps by a conversion factor, chosen to ensure that the resulting time series segments contains no less than 6 but no more than 9 X-class flares per 4000 model iterations, the width of our assimilation window in all results presented below. We carry out this manual adjustment separately for each active region in Table 2. This procedure, as minimalistic as it might be, at least captures intrinsic variations in flaring rates and peak energy release from one active region to another.

Figure 11 shows a representative example of the assimilation of GOES data for AR10808 and subsequent "all clear" forecast. Here the assimilation (left panel) properly captured 5 of 6 events in the assimilation, missing only the lowest energy event at iteration 1150, for a final cost function value of $\mathcal{J} = 0.0975$. The top right panel shows the temporal continuation of the GOES data, with our all-clear forecast window indicated in pink. The bottom right panel shows the superposition of 10000 forecasts produced using the assimilated initial condition. The three occurrence histograms shown (note the logarithmic vertical scale) are color coded according to total avalanche energy, as labeled. As in Figure 4, the presence of peaks indicated flaring behavior occurring at preferred times. During the first 125 iterations of the forecast model, no strong avalanche is produced, which is why the histograms are empty. Then 97.37% of forecasts do produce at least one avalanche within the forecast window. In contrast, the model climatological forecasts, using 10000 unassimilated initial conditions (thin line histogram), has a significantly lower success rate of 61.89%.

Figure 12, similar in format to Fig. 9, shows the true correct rate defined by eq. 11, against increasing threshold E^* in the energy of the target GOES flares over a forecast window of $T = 569$ iterations (left), and against forecast window width T at fixed threshold energy $E^* = 5 \times 10^6$ (right). Results are shown again for decreasing cost function cutoffs in the ensemble of assimilation runs retained in forecasting, as color-coded and labeled. For each assimilated initial condition retained in each ensemble for a given cost function cutoff value, 1000 forecasts are produced to generate the results displayed in the Figure. The model climatological forecast associated with 1000 forecasts for each one of 11 unassimilated initial conditions is again shown in blue. As with the forecasting of synthetic data discussed in the preceding section, forecasts of GOES flaring data based on assimilation outperform model climatology at all energy threshold values, but the improvement is greatest for flares in the middle of the plotted (logarithmic) range. As discussed previously, decreasing forecasting skills for small avalanches/flares is expected, as these are more strongly affected by the stochastic elements present in the model, with the associated lattice stress patterns not necessarily well represented by an eigenvalue decomposition retaining only the 50 highest-power modes.

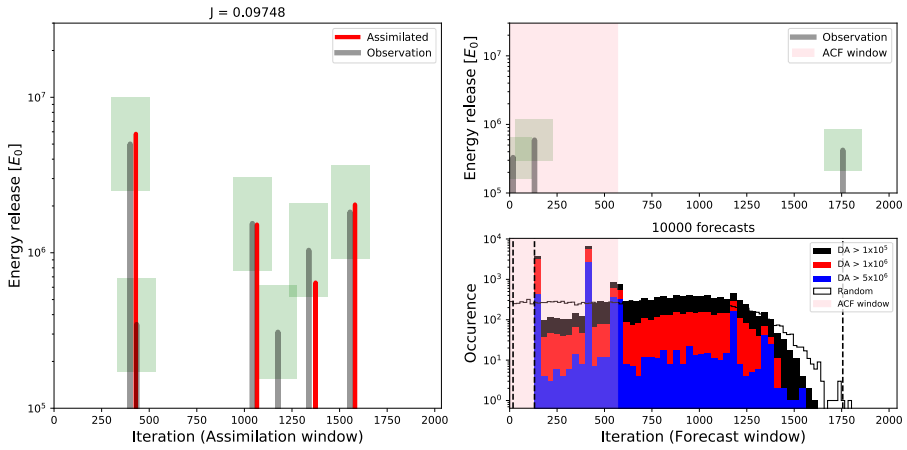

Figure 11. *Left*: Assimilation window results for a representative assimilation run using Model D01 (red) over GOES AR number 10808 compressed time series (grey). *Top right*: Forecast window for the GOES AR number 10808 time series. *Bottom right*: Composite temporal distribution of events in all 10000 forecasts produced from Model D01 following the assimilation window, varying only the random number seed for each forecast. The dash vertical lines represent the timing of the target observation. The pink area spans the width of the "All clear forecast" window.

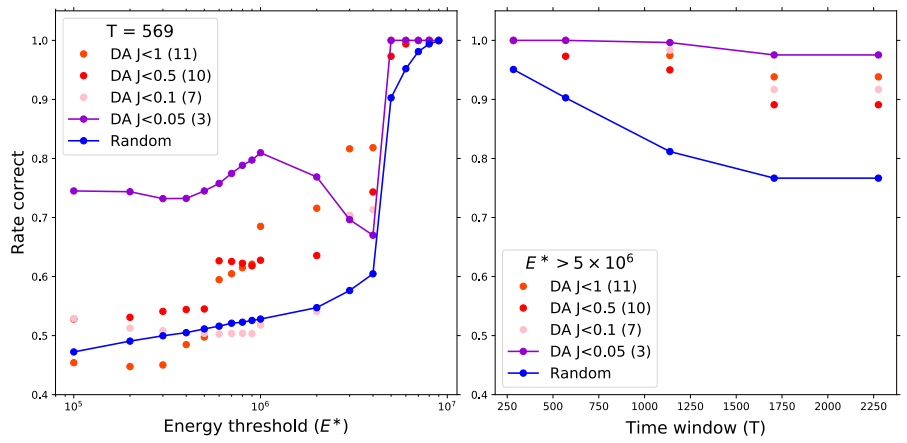

Figure 12. "All clear" forecasting performance on GOES data. The left panels shows the variation of our rate correct measure (eq. 11) as a function of target avalanche energy threshold over a forecasting window of $T = 569$ model iterations. The right panel shows an equivalent plot, but now as a function forecasting window a for fixed target avalanche energy threshold of $E^* = 5 \times 10^6$. The color scheme identifies the range of cost function values used to select assimilated initial conditions for forecasting, as labeled, with the corresponding number of members in each ensemble given in parentheses. As on Fig. 9, the blue dots and line give the model's climatological forecast.

6. Discussion and Conclusion

Lattice-based sandpile models of solar (and stellar) flares are a highly idealized representation of the processes of slow energy accumulation and rapid, instability-driven release in coronal magnetic fields structures, much along the lines of Parker (1988)'s nanoflare model. In this paper we have described a solar flare forecasting method based on assimilation of GOES X-Ray flux time series into a sandpile model. The fundamental idea underlying this approach harks back to a known feature of self-organized critical avalanche models, namely the presence of long-range correlations in avalanching behavior. More specifically, large avalanches release large-scale stress patterns established across the lattice by earlier avalanches, in particular large ones. As a consequence, while the triggering and unfolding of small avalanche is dominated by stochastic effects and thus effectively unpredictable, this is not necessarily so for the larger avalanches. In section 3 of this paper we demonstrated explicitly this somewhat counter-intuitive property of some self-organized critical sandpile models.

Distinct sandpile models can be constructed based upon specific choices of driving, stability threshold and redistribution rules. As demonstrated in §3, it turns out that such distinct model implementations exhibit widely varying levels of predictability even for the larger avalanches they generate. Of the three types of sandpile models tested, the more strongly non-conservative deterministically-driven models (model D01 herein) showed the longest predictability window. This in agreement with the earlier exploratory analysis presented in Strugarek and Charbonneau (2014). Stochastically-driven conservative models performed the worst, consistent with the results presented in Bélanger, Vincent, and Charbonneau (2007). Most pertinent for its forecasting potential, the predictability window of the D01 model was found to extend over 4 times the median inter-event wait time characterizing energy release in large events.

Data assimilation in sandpile models requires adjusting the initial lattice state so as to reproduce avalanching/flaring behavior in a pre-set assimilation window where observations are available. This defines an optimization problem, which turns out to be a very challenging one. The form of cost function being minimized leads to a search space that is multimodal and strongly degenerate, as a great number of lattice configurations can lead to similar temporal avalanching patterns. We opted for an iterative optimization approach based on ensemble trials of simulated annealing, which allows adequate and consistent minimization of the cost function measuring misfit between model predictions and data being assimilated. The computational speed of the sandpile model is essential for achieving this minimization in a reasonable amount of computing time.

After validating our forecasting scheme on synthetic data in §4.3, we then applied our method to the "all-clear" forecast problem, working off GOES X-Ray flux time series for 11 solar active regions having generated multiple X-class flares (§5). Our data assimilation scheme was shown to lead to a marked improvement in forecasting skill for the larger flares, as compared to the model's climatology. The latter was generated by simply skipping the data assimilation step, and running the forecasting step from an unassimilated initial condition randomly chosen from a reference run of the sandpile model. Such a forecast thus captures

the mean "flaring rate" of the model, and as such represents an appropriate form of baseline climatology in this context. Forecasting improvement is greatest for the largest flares/avalanches, provided these are not large to the point of being affected by the break of scale invariance produced by the finite size of the lattice.

These results are very encouraging, but numerous improvements are possible, and indeed are needed. Most pressing perhaps is to improve on the very simple rescaling procedure introduced here to match the flaring rates and peak energy release inferred from GOES X-Ray time series to the corresponding quantities in the sandpile model. In all models considered here, a statistically uniform flaring rate results from a constant or statistically stationary driving rate, leading to an inter-event waiting time distribution of exponential form. This is not the case for flaring on the Sun, but the observed waiting time distribution can be reproduced reasonably well by partitioning the data into contiguous blocks of constant flaring rates. (e.g. Wheatland 2000). Such non-uniform flaring rates are readily generated in sandpile models by modulating the driving process, which can lead to waiting-time distributions better aligned with observations (Norman *et al.*, 2001). Simultaneously matching model and observed two-dimensional distribution of events in waiting time and energy release is a promising avenue we are currently exploring. A proper scaling of energy and time between model and observation is also a prequisite to the calculation of a true skill score against observed flaring climatology (for more on this point see Barnes *et al.*, 2016, §3).

An important finding of the present study is the demonstration that not all self-organized critical sandpile models of solar flares have equal predictive potential, even though they may all match more or less equally well the observed power-law distributions of energy release in flares. Forecasting improvement may be achieved by identifying other sandpile models with even better predictive potential than our "best" model D01. Two candidates currently under examination are the fieldline-based model of Morales and Charbonneau (2008), and the energy minimizing lattice model of Farhang, Safari, and Wheatland (2018); Farhang, Wheatland, and Safari (2019).

There are inherent limitations to the flare forecasting scheme introduced here. Our data assimilation scheme requires a history of past flaring behavior for the active region being modeled, spanning a time interval of a few times the inverse flaring rate. This is quite different from many forecasting schemes that work off, say, line-of-sight or vector magnetograms of active regions, where in some cases a useful forecast can be produced from a single such magnetogram (see, e.g., the various forecasting schemes investigated in Leka *et al.* 2019a). Our approach should be viewed as complementary to these existing techniques, especially since its low computational requirements could allow rapid, near-real-time assessment of upcoming probable flaring activity of a given active region, to be then observed and assessed more closely with other methods.

Acknowledgements We thank A.S. Brun, L. Jouve and A. Vincent for multiple discussions on data assimilation procedures. We acknowledge the financial support from the Natural Sciences and Engineering Research Council of Canada (NSERC). C. Thibeault is supported in part by a merit scholarship from Hydro Québec. A. Strugarek thanks N. Vilmer and L. Klein for discussions on solar flares and self-organized criticality models. A. Strugarek acknowledges funding from ERC WHOLESUN 810218 grant, INSU/PNST, CNES Solar

Orbiter, and from the P2IO LabEx (ANR-10-LABX-0038) in the framework "Investissements d'Avenir" (ANR-11-IDEX-0003-01) managed by the Agence Nationale de la Recherche (ANR, France). This work used data provided by the MEDOC data and operations centre (CNES / CNRS / Univ. Paris-Saclay), http://medoc.ias.u-psud.fr/.

References

Aschwanden, M.: 2011, *Self-Organized Criticality in Astrophysics: The Statistics of Nonlinear Processes in the Universe*, *Astronomy and Planetary Sciences*, Springer, Berlin Heidelberg. ISBN 978-3-642-15000-5. DOI. https://www.springer.com/gp/book/9783642150005. [aschwanden_self-organized_2011]

Aschwanden, M.J.: 2013, Self-Organized Criticality Systems. *Self-Organized Criticality Systems, Edited by M.J. Aschwanden. e-book published by Open Academic Press, Berlin, Warsaw, 2013, 483pp.* http://adsabs.harvard.edu/abs/2013socs.book.....A. [aschwanden_self-organized_2013]

Aschwanden, M.J., Freeland, S.L.: 2012, Automated Solar Flare Statistics in Soft X-Rays over 37 Years of GOES Observations: The Invariance of Self-organized Criticality during Three Solar Cycles. *The Astrophysical Journal* **754**, 112. ADS Bibcode: 2012ApJ...754..112A. DOI. https://ui.adsabs.harvard.edu/abs/2012ApJ...754..112A. [aschwanden_automated_2012]

Aschwanden, M.J., Stern, R.A., Güdel, M.: 2008, Scaling laws of solar and stellar flares. *The Astrophysical Journal* **672**(1), 659. arXiv: 0710.2563. DOI. http://arxiv.org/abs/0710.2563. [aschwanden_scaling_2008]

Aschwanden, M.J., Crosby, N.B., Dimitropoulou, M., Georgoulis, M.K., Hergarten, S., McAteer, J., Milovanov, A.V., Mineshige, S., Morales, L., Nishizuka, N., Pruessner, G., Sanchez, R., Sharma, A.S., Strugarek, A., Uritsky, V.: 2016, 25 Years of Self-Organized Criticality: Solar and Astrophysics. *Space Science Reviews* **198**(1-4), 47. DOI. http://link.springer.com/10.1007/s11214-014-0054-6. [aschwanden_25_2016]

Bak, P., Tang, C., Wiesenfeld, K.: 1987, Self-organized criticality: An explanation of the 1/f noise. *Physical Review Letters* **59**(4), 381. Publisher: American Physical Society. DOI. https://link.aps.org/doi/10.1103/PhysRevLett.59.381. [bak_self-organized_1987]

Barnes, G., Leka, K.D.: 2008, Evaluating the Performance of Solar Flare Forecasting Methods. *Astrophys. J. Lett.* **688**(2), L107. DOI. ADS. [2008ApJ...688L.107B]

Barnes, G., Leka, K.D., Schrijver, C.J., Colak, T., Qahwaji, R., Ashamari, O.W., Yuan, Y., Zhang, J., McAteer, R.T.J., Bloomfield, D.S., Higgins, P.A., Gallagher, P.T., Falconer, D.A., Georgoulis, M.K., Wheatland, M.S., Balch, C., Dunn, T., Wagner, E.L.: 2016, A Comparison of Flare Forecasting Methods, I: Results from the "All-Clear" Workshop. *The Astrophysical Journal* **829**(2), 89. arXiv: 1608.06319. DOI. http://arxiv.org/abs/1608.06319. [barnes_comparison_2016]

Bélanger, E., Vincent, A., Charbonneau, P.: 2007, Predicting Solar Flares by Data Assimilation in Avalanche Models. *Solar Physics* **245**(1), 141. DOI. https://doi.org/10.1007/s11207-007-9009-3. [belanger_predicting_2007]

Charbonneau, P., Mcintosh, S., Liu, H., Bogdan, J.: 2001, Avalanche models for solar flares (Invited Review). *Solar Physics*, 321. DOI. https://opensky.ucar.edu/islandora/object/articles%3A8921/. [charbonneau_avalanche_2001]

Cheung, M.C.M., Rempel, M., Chintzoglou, G., Chen, F., Testa, P., Martínez-Sykora, J., Sainz Dalda, A., DeRosa, M.L., Malanushenko, A., Hansteen, V., De Pontieu, B., Carlsson, M., Gudiksen, B., McIntosh, S.W.: 2019, A comprehensive three-dimensional radiative magnetohydrodynamic simulation of a solar flare. *Nature Astronomy* **3**, 160. DOI. http://adsabs.harvard.edu/abs/2019NatAs...3..160C. [cheung_comprehensive_2019]

Dennis, B.R.: 1985, Solar hard X-ray bursts. *Solar Physics* **100**, 465. DOI. http://adsabs.harvard.edu/abs/1985SoPh..100..465D. [dennis_solar_1985]

Farhang, N., Safari, H., Wheatland, M.S.: 2018, Principle of Minimum Energy in Magnetic Reconnection in a Self-organized Critical Model for Solar Flares. *The Astrophysical Journal* **859**(1), 41. Publisher: American Astronomical Society. DOI. https://doi.org/10.3847%2F1538-4357%2Faac01b. [farhang_principle_2018]

Farhang, N., Wheatland, M.S., Safari, H.: 2019, Energy Balance in Avalanche Models for Solar Flares. *The Astrophysical Journal* **883**(1), L20. Publisher: American Astronomical Society. DOI. https://doi.org/10.3847%2F2041-8213%2Fab40c3. [farhang_energy_2019]

Hung, C.P., Brun, A.S., Fournier, A., Jouve, L., Talagrand, O., Zakari, M.: 2017, Variational estimation of the large scale time dependent meridional circulation in the Sun: proofs of concept with a solar mean field dynamo model. *The Astrophysical Journal* **849**(2), 160. arXiv: 1710.02114. DOI. http://arxiv.org/abs/1710.02114. [hung_variational_2017]

Jensen, H.J.: 1998, *Self-Organized Criticality: Emergent Complex Behavior in Physical and Biological Systems*, 1 edition edn. Cambridge University Press, Cambridge ; New York. ISBN 978-0-521-48371-1. [jensen_self-organized_1998]

Kalnay, E.: 2002, *Atmospheric Modeling, Data Assimilation and Predictability*, 1 edition edn. Cambridge University Press, New York. ISBN 978-0-521-79629-3. [kalnay_atmospheric_2002]

Leka, K.D., Park, S.-H., Kusano, K., Andries, J., Barnes, G., Bingham, S., Bloomfield, D.S., McCloskey, A.E., Delouille, V., Falconer, D., Gallagher, P.T., Georgoulis, M.K., Kubo, Y., Lee, K., Lee, S., Lobzin, V., Mun, J., Murray, S.A., Nageem, T.A.M.H., Qahwaji, R., Sharpe, M., Steenburgh, R.A., Steward, G., Terkildsen, M.: 2019a, A Comparison of Flare Forecasting Methods. II. Benchmarks, Metrics, and Performance Results for Operational Solar Flare Forecasting Systems. *The Astrophysical Journal Supplement Series* **243**(2), 36. Publisher: American Astronomical Society. DOI. https://doi.org/10.3847%2F1538-4365%2Fab2e12. [leka_comparison_2019]

Leka, K.D., Park, S.-H., Kusano, K., Andries, J., Barnes, G., Bingham, S., Bloomfield, D.S., McCloskey, A.E., Delouille, V., Falconer, D., Gallagher, P.T., Georgoulis, M.K., Kubo, Y., Lee, K., Lee, S., Lobzin, V., Mun, J., Murray, S.A., Nageem, T.A.M.H., Qahwaji, R., Sharpe, M., Steenburgh, R., Steward, G., Terkildsen, M.: 2019b, A Comparison of Flare Forecasting Methods. III. Systematic Behaviors of Operational Solar Flare Forecasting Systems. *The Astrophysical Journal* **881**(2), 101. arXiv: 1907.02909. DOI. http://arxiv.org/abs/1907.02909. [leka_comparison_2019-1]

Liu, W.W., Charbonneau, P., Thibault, K., Morales, L.: 2006, Energy avalanches in the central plasma sheet. *Geophysical Research Letters* **33**(19). _eprint: https://agupubs.onlinelibrary.wiley.com/doi/pdf/10.1029/2006GL027282. DOI. https://agupubs.onlinelibrary.wiley.com/doi/abs/10.1029/2006GL027282. [liu_energy_2006]

Lu, E.T., Hamilton, R.J.: 1991, Avalanches and the distribution of solar flares. *The Astrophysical Journal Letters* **380**, L89. DOI. http://adsabs.harvard.edu/abs/1991ApJ...380L..89L. [lu_avalanches_1991]

Lu, E.T., Hamilton, R.J., McTiernan, J.M., Bromund, K.R.: 1993, Solar flares and avalanches in driven dissipative systems. *The Astrophysical Journal* **412**, 841. DOI. http://adsabs.harvard.edu/abs/1993ApJ...412..841L. [lu_solar_1993]

Morales, L., Charbonneau, P.: 2008, Self-organized Critical Model of Energy Release in an Idealized Coronal Loop. *The Astrophysical Journal* **682**(1), 654. Publisher: IOP Publishing. DOI. https://iopscience.iop.org/article/10.1086/588274/meta. [morales_self-organized_2008]

Morales, L.F., Santos, N.A.: 2020, Predicting Extreme Solar Flare Events Using Lu and Hamilton Avalanche Model. *Solar Phys.* **295**(11), 155. DOI. ADS. [2020SoPh..295..155M]

Namekata, K., Sakaue, T., Watanabe, K., Asai, A., Maehara, H., Notsu, Y., Notsu, S., Honda, S., Ishii, T.T., Ikuta, K., Nogami, D., Shibata, K.: 2017, Statistical Studies of Solar White-light Flares and Comparisons with Superflares on Solar-type Stars. *The Astrophysical Journal* **851**, 91. DOI. http://adsabs.harvard.edu/abs/2017ApJ...851...91N. [namekata_statistical_2017]

Norman, J.P., Charbonneau, P., McIntosh, S.W., Liu, H.-L.: 2001, Waiting-Time Distributions in Lattice Models of Solar Flares. *The Astrophysical Journal* **557**, 891. DOI. http://adsabs.harvard.edu/abs/2001ApJ...557..891N. [norman_waiting-time_2001]

Olami, Z., Feder, H.J.S., Christensen, K.: 1992, Self-organized criticality in a continuous, non-conservative cellular automaton modeling earthquakes. *Physical Review Letters* **68**(8), 1244. Publisher: American Physical Society. DOI. https://link.aps.org/doi/10.1103/PhysRevLett.68.1244. [olami_self-organized_1992]

Parker, E.N.: 1988, Nanoflares and the solar X-ray corona. *The Astrophysical Journal* **330**, 474. DOI. http://adsabs.harvard.edu/abs/1988ApJ...330..474P. [parker_nanoflares_1988]

Pascual, V., Hascoët, L.: 2006, Extension of TAPENADE toward Fortran 95. In: Bücker, M., Corliss, G., Naumann, U., Hovland, P., Norris, B. (eds.) *Automatic Differentiation: Applications, Theory, and Implementations*, *Lecture Notes in Computational Sci-*

ence and Engineering, Springer, Berlin, Heidelberg, 171. ISBN 978-3-540-28438-3. DOI. [pascual_extension_2006]

Press, W.H., Flannery, B.P., Teukolsky, S.A., Vetterling, W.T.: 1992, *Numerical Recipes in FORTRAN 77: Volume 1, Volume 1 of Fortran Numerical Recipes: The Art of Scientific Computing*. [press_numerical_1992]

Strugarek, A., Charbonneau, P.: 2014, Predictive Capabilities of Avalanche Models for Solar Flares. *Solar Physics* **289**(11), 4137. DOI. https://doi.org/10.1007/s11207-014-0570-2. [strugarek_predictive_2014]

Strugarek, A., Charbonneau, P., Joseph, R., Pirot, D.: 2014, Deterministically Driven Avalanche Models of Solar Flares. *Solar Physics* **289**(8), 2993. DOI. https://doi.org/10.1007/s11207-014-0509-7. [strugarek_deterministically_2014]

Strugarek, A., Brun, A.S., Charbonneau, P., Vilmer, N.: 2017, Sandpile Models and Solar Flares: Eigenfunction Decomposition for Data Assimilation. *Proceedings of the International Astronomical Union* **13**(S335), 250. Publisher: Cambridge University Press. DOI. https://www.cambridge.org/core/journals/proceedings-of-the-international-astronomical-union/article/sandpile-models-and-solar-flares-eigenfunction-decomposition-for-data-assimilation/6217C836E893573DEE272CB39A5CCEE5. [strugarek_sandpile_2017]

Vallières-Nollet, M.-A., Charbonneau, P., Uritsky, V., Donovan, E., Liu, W.: 2010, Dual scaling for self-organized critical models of the magnetosphere. *Journal of Geophysical Research: Space Physics* **115**(A12). _eprint: https://agupubs.onlinelibrary.wiley.com/doi/pdf/10.1029/2010JA015641. DOI. https://agupubs.onlinelibrary.wiley.com/doi/abs/10.1029/2010JA015641. [vallieresnollet_dual_2010]

Watkins, N.W., Pruessner, G., Chapman, S.C., Crosby, N.B., Jensen, H.J.: 2016, 25 Years of Self-organized Criticality: Concepts and Controversies. *Space Sci. Rev.* **198**(1-4), 3. DOI. ADS. [2016SSRv..198....3W]

Wheatland, M.S.: 2000, The Origin of the Solar Flare Waiting-Time Distribution. *The Astrophysical Journal Letters* **536**, L109. DOI. http://adsabs.harvard.edu/abs/2000ApJ...536L.109W. [wheatland_origin_2000]